Micromagnetic modeling of SOT-MRAM dynamics

Nils Petter Jørstad [a],[*], Simone Fiorentini [a],[b], Johannes Ender [a],[b], Wolfgang Goes [c], Siegfried Selberherr [b], Viktor Sverdlov [a],[b]

[a] *Christian Doppler Laboratory for Nonvolatile Magnetoresistive Memory and Logic at the Institute for Microelectronics, TU Wien, Gußhausstraße 27-29, A-1040, Vienna, Austria*
[b] *Institute for Microelectronics, TU Wien, Gußhausstraße 27-29, A-1040, Vienna, Austria*
[c] *Silvaco Europe Ltd., Cambridge, United Kingdom*

ARTICLE INFO

ABSTRACT

We present a flexible and efficient approach to modeling the magnetization dynamics in modern SOT-MRAM cells, by coupling charge, spin, and magnetization dynamics in a three-dimensional framework. We expand on existing literature, to obtain spin current boundary conditions for modeling the Rashba-Edelstein effect. We compute the spin–orbit torques originating from both, the spin Hall and Rashba-Edelstein effect, and show that our model can reproduce experimental results for the thickness dependence of the spin torques in an Ir/CoFeB bilayer structure. Furthermore, we verify our approach by simulating magnetization reversal in field-free SOT-MRAM cells, and show that with the inclusion of the interfacial Dzyaloshinskii–Moriya interaction, we obtain domain wall motion similar to previously reported experimental results.

1. Introduction

Spin–orbit torque magnetoresistive random access memory (SOT-MRAM) devices offer an attractive alternative to traditional memory technology due to their non-volatility, low power consumption, high switching speed, and long endurance. SOT-MRAM possesses a nearly unlimited endurance compared to the well established spin-transfer torque (STT) MRAM, due to the separation of the read and write paths. In addition, it offers a roughly one order of magnitude faster writing speeds, achieved by taking advantage of the spin–orbit coupling (SOC). As it is a three-terminal device, the large footprint limits the applications to cache memories, where its sub-ns writing speeds and long endurance make it a good potential non-volatile replacement for current SRAM devices [1–3].

The basic SOT-MRAM cell consists of a magnetic tunnel junction (MTJ), a three layer structure where two ferromagnetic (FM) layers are separated by a tunneling barrier (TB), placed on a heavy metal (HM) line as illustrated in Fig. 1. The upper and lower FM layers are called the reference layer (RL) and the free layer (FL), respectively, as the magnetization is fixed in the RL and can be changed in the FL. The logical state of the cell is encoded in the relative orientation of the magnetization of the two layers, which can be either parallel or anti-parallel. Due to the tunnel magnetoresistance (TMR), the resistance across the MTJ can be significantly higher, when the MTJ is in the anti-parallel state compared to the parallel state, enabling easy reading

of the state. The state of the cell is written electrically by applying a current across the HM layer. The current passing through the HM becomes spin-polarized through the spin Hall effect (SHE) [4]. The resulting spin currents are perpendicular to the current direction and are injected into the adjacent FL, where the spins quickly align with the magnetization direction. Due to the conservation of angular momentum, the magnetization experiences a torque corresponding to the absorbed transverse spin current, allowing for efficient manipulation of the magnetization. Another source of spin torques is the HM/FM interface, where the Rashba spin–orbit coupling (SOC) lifts the spin degeneracy of the band structure, locking the spin to the in-plane momentum. When an in-plane electric field is applied, the occupancy is shifted and a non-equilibrium spin accumulation is generated through the Rashba-Edelstein effect (REE) [5].

The symmetry of the SOTs originating from the SHE and the REE introduces challenges for designing SOT-MRAM cells with perpendicular magnetization orientation, which are required to achieve appropriate densities for memory applications. As both effects generate SOTs which act to bring the magnetization in-plane, out-of-plane switching of the FL requires additional assistance. This has been typically achieved with an external magnetic field along the current direction, however, as this limits scaling and complicates the circuit architecture, so-called field-free approaches have been favored instead. Several field-free solutions have been proposed and demonstrated, some requiring built-in
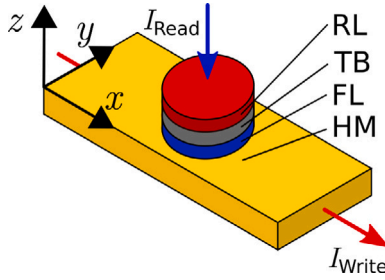

Fig. 1. An illustration of a typical SOT-MTJ. The RL, TB, FL, and HM are shown in red, gray, blue, and yellow, respectively. The blue arrow shows the direction of the read current, and the red arrow shows the direction of the write current.

Fig. 2. A schematic of the considered interface scattering system. An interface at $z = 0$ separates a HM layer at $z = 0^-$ from a FM layer at $z = 0^+$. Localized at the interface is a spin-dependent potential with an effective field $\mathbf{u_{eff}}$. The local basis is aligned with the interface normal, while the spin basis is aligned with the effective field at the interface.

magnetic fields [6], additional symmetry-breaking layers [7], or the combination of SOT with STT [8].

To overcome the engineering challenges and to accelerate the development and adoption of SOT-MRAM devices, there is a demand for software capable of fast and accurate exploration of their design space. We present results from a finite element micromagnetic simulator, developed with the goal to simulate FL magnetization reversal in realistic multi-layer, multi-terminal SOT- and STT-MRAM devices. The spin torques acting on the FL are calculated by solving coupled spin and charge drift-diffusion equations with appropriate boundary conditions. The HM/FL interface receives special attention to accurately model spin torques originating from both the SHE and the REE.

This work goes beyond similar approaches by including all the relevant physical effects, such as the SHE, REE, and interfacial Dzyaloshinskii–Moriya interaction (iDMI), in one unified model connecting spin, charge, and magnetization dynamics. The equations are solved using the finite element method (FEM), allowing for proper flexibility in mesh geometries. We can compute the redistribution of the currents and spin accumulation in realistic multi-layer structures in order to obtain the spin torque acting on the local magnetization in the FM layers. With unique boundary conditions for the tunneling spin current and interfacial SOC we can model the local effects of MTJs during switching and reproduce experimental measurements for the SOTs, respectively.

In the next section we combine and build on the semi-classical approaches presented in [9,10] to obtain proper models for the transverse spin current and torque contributions generated through the interfacial Rashba SOC. The expressions for interfacial spin and charge current from [10] are generalized for any direction of the magnetization, and analytical formulae for the interface scattering matrices are derived. The resulting expressions come in the form of boundary conditions for the drift-diffusion equations for spin. In Section 3 we present the drift-diffusion model to compute the spin accumulation and spin torques in SOT-MRAM. In Section 4, we present the micromagnetic model employed to model the magnetization dynamics of the FL. In Section 5 we briefly explain the numerical implementation and combination of the drift-diffusion and micromagnetic equations. In Section 6 we reproduce the experimental thickness dependence of the torques in a HM/FM bilayer structure using our model. In Section 7 we present the magnitude and symmetry of the SOTs obtained with our approach. Finally, we prove the flexibility of our approach by presenting simulation results for anti-parallel to parallel (APP) and parallel to anti-parallel (PAP) switching of the FL for two different field-free SOT-MRAM cells, in Sections 8 and 9.

2. Spin transport at interfaces with SOC

We consider a HM/FM interface in the x–y plane at $z = 0$, with the HM below ($z = 0^-$) and FM above ($z = 0^+$) the interface. The scattering system is depicted in Fig. 2. We treat the interface as a spin-dependent delta function potential and assume specular plane-wave scattering of the electrons from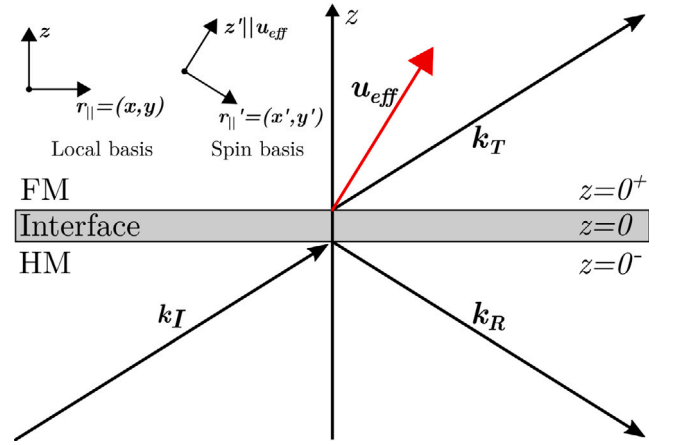 the interface. For simplicity we assume a weak exchange splitting in the bulk of the FM compared to the interface, and we describe the bulk on either side of the interface as a spin-independent free electron gas with a spherical Fermi surface in equilibrium. With these assumptions there is no explicit difference between the HM and FM side of the interface.

The plane-wave solution 2×2 Hamiltonian describing the system is then given by [10]:

$$H(\mathbf{r}, \mathbf{k}) = \frac{\hbar^2 k^2}{2m} I_{2\times2} + \frac{\hbar^2 k_F}{m} \delta(z) \left(u_0 I_{2\times2} + \boldsymbol{\sigma} \cdot \mathbf{u_{eff}}(\mathbf{k}) \right) \quad (1)$$

$\boldsymbol{\sigma} = (\sigma_x, \sigma_y, \sigma_z)$ is a vector of the Pauli matrices, u_0 is the dimensionless magnitude of the spin-independent part of the potential, and $\mathbf{u_{eff}}$ is a dimensionless effective magnetic field at the interface. $\hbar$ is the reduced planck's constant, m is the electron mass, and k is the wave number of the incident plane waves. $I_{2\times2}$ is the 2×2 identity matrix. The factor $\hbar^2 k_F \delta(z)/m$ converts the dimensionless potentials u_0 and $\mathbf{u_{eff}}$ into units of energy, where k_F is the Fermi wave number.

We describe the effective field as a combination of an exchange interaction and a Rashba SOC at the interface:

$$\mathbf{u_{eff}}(\mathbf{k}) = u_{ex} \mathbf{m} + u_R \hat{\mathbf{z}} \times \frac{\mathbf{k}}{k_F} \quad (2)$$

The dimensionless parameters u_{ex} and u_R are the magnitudes of the exchange and Rashba spin–orbit interactions, respectively, and $\mathbf{m}$ is the magnetization direction at the interface. Other forms of interfacial SOC such as a Dresselhaus type spin–orbit interaction can also be included in $\mathbf{u_{eff}}$ [11].

We set the quantization axis along the effective field and consider a plane wave spinor incident on the interface. The reflected and transmitted spinors can then be related to the incident one through the scattering matrices

$$r = \begin{pmatrix} r_\uparrow & 0 \\ 0 & r_\downarrow \end{pmatrix} \quad (3)$$

and

$$t = \begin{pmatrix} t_\uparrow & 0 \\ 0 & t_\downarrow \end{pmatrix} \quad (4)$$

for reflection and transmission, respectively. Using the boundary conditions for the continuity of the wave function and the probability current at $z = 0$, the following scattering amplitudes are obtained [12,13]:

$$r_{\uparrow/\downarrow} = \frac{u_{\uparrow/\downarrow}}{ik_z/k_F - u_{\uparrow/\downarrow}} \quad (5)$$

$$t_{\uparrow/\downarrow} = \frac{ik_z/k_F}{ik_z/k_F - u_{\uparrow/\downarrow}} \tag{6}$$

$u_{\uparrow/\downarrow} = u_0 \pm u_{\text{Eff}}$, and k_z is the out-of-plane component of the wave vector.

In order to obtain semi-classical boundary conditions for either the drift-diffusion or Boltzmann equations, matrices describing the scattering of an ensemble of spins with polarization s and charge c are required. Following the derivation in [9] one arrives at

$$\overline{R}_{\alpha\beta} = \frac{1}{2} \text{Tr} \left[r^\dagger \sigma_\alpha r \sigma_\beta \right] \tag{7}$$

and

$$\overline{T}_{\alpha\beta} = \frac{1}{2} \text{Tr} \left[t^\dagger \sigma_\alpha t \sigma_\beta \right], \tag{8}$$

where $\alpha, \beta \in \{s, c\}$, $(\cdot)^\dagger$ denotes the conjugate transpose, and Tr denotes the trace operator. σ_s are the Pauli matrices for $s \in \{x', y', z'\}$, which denotes the spin polarization along the Cartesian axes in a spin basis with $\mathbf{z}' = \mathbf{u_{eff}}$. σ_c is the 2×2 identity matrix, where c denotes charge. The bar above the matrices denotes that the spin polarization is defined according to the spin basis.

$\overline{R}$ and $\overline{T}$ constitute 4×4 scattering matrices describing the probability of an incident ensemble of spins with polarization β, reflecting and transmitting into polarization α, respectively. The matrices can be used to obtain boundary conditions for the non-equilibrium distribution function in the Boltzmann equation [10]. The resulting matrices from computing the traces with the scattering amplitudes in Eqs. (5), (6) are given in detail in Appendix A.

We consider a non-equilibrium Boltzmann distribution function for spin and charge $g_\alpha^I(0^\pm, \mathbf{k}^\mp)$, incident from above and below the surface with the wave vector $\mathbf{k}^\pm = (k_x, k_y, \pm k_z)$. With the scattering matrices, we can describe the total density functions on either side of the interface in terms of the incident ones. Multiplying these density functions with the velocity along z and integrating over the Fermi surface we obtain boundary conditions for the spin and charge currents on either side of the interface, which can be applied to the drift-diffusion equations. In units of charge current density (A/m^2), the out-of-plane spin-charge four-vector currents above and below the interface are given by [10]:

$$\tilde{j}_z(0^\pm) = \frac{\mp e}{\hbar(2\pi)^3} \int_{\text{FS} \in \text{in}} d\mathbf{k} \frac{k_z}{k_F}$$
$$\times \left[\left(I_{4\times4} - R(\mathbf{k}) \right) \tilde{g}^I(0^\pm, \mathbf{k}) - T(\mathbf{k}) \tilde{g}^I(0^\mp, \mathbf{k}) \right] \tag{9}$$

e is the elementary charge, $I_{4\times4}$ is the 4×4 identity matrix, and the integration is performed over the incident part of the Fermi surface. Here and from now on the tilde symbol above a quantity denotes a four-dimensional vector. As the matrices were derived in a spin frame with $\hat{z}' = \mathbf{u_{ueff}}$, an orthogonal transformation is necessary in order to describe the spin currents in the local frame with $\mathbf{z}$ along the interface normal. The orthogonal transformation

$$S(\mathbf{k}) = O^{\text{T}}(\mathbf{k}) \bar{S}(\mathbf{k}) O(\mathbf{k}) \tag{10}$$

is performed on all scattering matrices to convert them from the spin basis to the local basis, where $O(\mathbf{k})$ is the coordinate transformation matrix and $O^{\text{T}}(\mathbf{k})$ is its transpose. The form of $O(\mathbf{k})$ is presented in Appendix B.

We consider in-plane spin/charge currents driving out-of-plane spin/charge current through the SOC. The interfacial SOC can also generate in-plane spin and charge currents, however, these are assumed to weakly affect the torques and are left for future work to consider. Out-of-plane currents driven by spin/charge chemical potentials V_α at $z = 0^\pm$ can also be captured with (9) by considering $g_\alpha^I(0^\pm, \mathbf{k}) \approx eV_\alpha(0^\pm)$ [14]. Then, the integration can be performed over the scattering matrices only, resulting in interface conductance tensors for spin and charge, where the transverse directions contain computed spin-mixing conductances. We instead choose to capture the potential-driven transport through magnetoelectronic circuit theory [15], where the dependence on the magnetization direction is simple and the

interface conductances can be extracted from experiments or computed from first-principles. We present the boundary conditions for potential-driven interface transport in the next section.

For the case of in-plane spin/charge currents generating out-of-plane current, we approximate the incoming spin/charge density functions below and above the interface as [10]

$$g_\alpha^I(0^\pm, \mathbf{k}) = e \frac{k_x}{k_F} v_F \tau^\pm P_\alpha^\pm E_{\text{ip}}, \tag{11}$$

where without loss of generality an in-plane current along the x-direction has been assumed. v_F is the Fermi velocity, $\tau^\pm$ are momentum relaxation times in the HM/FM, $P_\alpha^\pm$ are dimensionless polarizations, and E_{ip} is the in-plane electric field. We describe the polarization above and below the interface as follows [9]

$$P_\alpha^\pm = \begin{cases} (\delta_{\alpha c} - \beta_\sigma \delta_{\alpha s} \hat{m}_s), & z = 0^+ \\ \delta_{\alpha c}, & z = 0^-, \end{cases} \tag{12}$$

where $\beta_\sigma = (\sigma_\uparrow^{\text{FM}} - \sigma_\downarrow^{\text{FM}})/(\sigma_\uparrow^{\text{FM}} + \sigma_\downarrow^{\text{FM}})$ is the current spin-polarization inside the FM, with $\sigma_{\uparrow/\downarrow}^{\text{FM}}$ being the bulk conductivity of majority/minority carriers. We can then write the currents at the interface in terms of conductivity tensors as

$$\tilde{j}_z(0^-) = \tilde{\sigma} E_{ip}$$
$$\tilde{j}_z(0^+) = \tilde{\gamma}^{\text{FM}} E_{ip}, \tag{13}$$

where

$$\tilde{\sigma} = \frac{e^2}{\hbar(2\pi)^3} \int_{\text{FS} \in \text{in}} d\mathbf{k} \frac{k_z k_x}{k_F^2}$$
$$\times \left[\left(I_{4\times4} - R(\mathbf{k}) \right) \tau^- \tilde{P}^- - T(\mathbf{k}) \tau^+ \tilde{P}^+ \right]. \tag{14}$$

is the conductivity tensor, and

$$\tilde{\gamma}^{\text{FM}} = \frac{e^2}{\hbar(2\pi)^3} \int_{\text{FS} \in \text{in}} d\mathbf{k} \frac{k_z k_x}{k_F^2}$$
$$\times \left[T(\mathbf{k}) \tau^- \tilde{P}^- - \left(I_{4\times4} - R(\mathbf{k}) \right) \tau^+ \tilde{P}^+ \right]. \tag{15}$$

is the bulk torkivity tensor. In Eq. (13) $j_{cz}(0^-) = j_{cz}(0^+)$, ensuring the continuity of the charge current. However, the spin components of the currents are discontinuous across the interface, as a result of the spin-flip scattering from the interface potential. The spin-flip scattering at the interface can be interpreted as a precession of the phase-coherent spin density around the effective field $\mathbf{u_{eff}}$ in a zero-thickness region at the interface. The precession around the exchange interaction part of the field ($u_{\text{ex}}\mathbf{m}$) describes a transfer of spin angular momentum to the local magnetization, resulting in an interfacial spin torque. The precession around the SOC part of the field ($u_R \hat{z} \times \hat{k}$), called spin–orbit precession, describes a parasitic loss of spin angular momentum to the lattice [9,10]. In the limit of zero interfacial SOC ($u_R \to 0$), this interfacial torque and the tensors given by (14) and (15) vanish.

The spin torque arising from interfacial SOC can be separated into two contributions, one acting on the magnetization at the interface through the interfacial exchange interaction, and the other one acting on the magnetization in the bulk. In the FM the transverse spins become aligned with the magnetization through a precession and dephasing process, and the magnetization experiences a torque due to the conservation of angular momentum. Assuming this process happens over a short distance from the interface, we can describe the latter contribution entirely with the transverse spin current on the FM side of the interface $\mathbf{j}_{\text{sz}}^\perp (0^+)$ [9,12]. The other contribution comes from the phase-coherent spin density at $z = 0$ interacting with the interface magnetization through the exchange coupling. The spin torque originating from the interfacial SOC acting on the magnetization at the interface is described by [9]:

$$\tau_s^{\text{mag}} = \frac{J_{ex}}{\hbar} \mathbf{s_0} \times \mathbf{m} \delta(0) = \gamma_s^{\text{mag}} E_{\text{ip}} \delta(0) \tag{16}$$

$\mathbf{s_0}$ is the phase-coherent spin density at $z = 0$ and J_{ex} is the exchange energy at the interface. γ_s^{mag} is an interfacial torkivity tensor describing

the torque from the interfacial exchange interaction. The subscript s denotes the spin part of the four-dimensional vectors. The interfacial torkivity tensor is given by [9]:

$$\gamma_s^{\text{mag}} = \mathbf{m} \times \left(\frac{u_{ex}e^2}{\hbar(2\pi)^3} \int_{\text{FS}\in\text{in}} d\mathbf{k} \frac{k_x}{k_F} T(\mathbf{k}) \left[\tau^- \tilde{P}^- + \tau^+ \tilde{P}^+ \right] \right)_s \tag{17}$$

Until now, we have assumed the interface normal $\mathbf{n}$ to be along $\hat{\mathbf{z}}$ and the in-plane electric field $\mathbf{E_{ip}}$ to be along $\hat{\mathbf{x}}$. In order to generalize the expressions for the conductivity and torkivity tensors for any $\mathbf{n}$ and $\mathbf{E_{ip}}$, additional orthogonal transformations are required between the laboratory frame and the frame aligned with the interface normal and the in-plane electric field. The details of this transformation are presented in Appendix C.

3. Coupled spin & charge model

The charge current density $\mathbf{J_c}$ in multi-layered structures consisting of non-magnetic (NM), FM and HM layers can be expressed as [16,17]:

$$\mathbf{J_C} = \sigma\mathbf{E} + \frac{e}{\mu_B}\beta_D D_e (\nabla S)^{\text{T}} \mathbf{m} + \theta_{\text{SHA}} D_e \frac{e}{\mu_B}\nabla \times \mathbf{S}, \tag{18}$$

The first term is Ohm's law, the second is the giant-magneto-resistance contribution in FM layers, and the third is the inverse SHE contribution in HM layers. σ, β_D, D_e, and θ_{SHA} are the conductivity, diffusion polarization, diffusion constant, and spin Hall angle, respectively. $(\nabla S)_{ij} = \partial S_i/\partial x_j$ is the vector gradient of the spin accumulation $\mathbf{S}$. The spin current tensor $(J_S)_{ij}$, describing flow of spin polarization i along direction j, is given by [16,17]:

$$J_S = -\frac{\mu_B}{e}\beta_\sigma \mathbf{m} \otimes (\sigma\mathbf{E}) - D_e\nabla S - \theta_{\text{SHA}}\frac{\mu_B}{e}\varepsilon(\sigma\mathbf{E}) \tag{19}$$

The first term describes the contribution from magnetization polarized currents in FM layers, the second term describes the diffusion of spins, and the last describes the SHE contribution in HM layers. ε_{ijk} is the Levi-Civita tensor.

We rewrite the spin current as a function of the charge current yielding

$$J_S = -\frac{\mu_B}{e}\beta_\sigma \mathbf{m} \otimes \left(\mathbf{J_c} - \frac{e}{\mu_B}\beta_D D_e (\nabla S)^{\text{T}} \mathbf{m} \right) - D_e\nabla S - \theta_{\text{SHA}}\frac{\mu_B}{e}\varepsilon \mathbf{J_c}, \tag{20}$$

where we have omitted terms containing θ_{SHA}^2.

The spin accumulation $\mathbf{S}$ is obtained from solving the steady-state continuity equation [12,18]

$$\frac{\partial \mathbf{S}}{\partial t} = 0 = -\nabla J_S - D_e \left(\frac{\mathbf{S}}{\lambda_{sf}^2} + \frac{\mathbf{S} \times \mathbf{m}}{\lambda_J^2} + \frac{\mathbf{m} \times (\mathbf{S} \times \mathbf{m})}{\lambda_\varphi^2} \right), \tag{21}$$

together with the spin current Eq. (20). λ_{sf}, λ_J, and λ_ϕ are the spin-flip, exchange, and dephasing lengths, respectively. As we are primarily interested in the magnetization dynamics, which happen at timescales three orders of magnitude slower compared to spin dynamics (typically $\sim$ ns for the former and $\sim$ ps for the latter [19]), we can assume that the spin accumulation immediately relaxes to the change in magnetization. This assumption was confirmed by [20] to be a valid approximation for similar systems.

The charge current density is obtained by solving the Laplace equation

$$\nabla \cdot (\sigma\nabla V) = 0 \tag{22}$$

for the electrical potential V together with the relation

$$\mathbf{J_C} = -\sigma\nabla V. \tag{23}$$

We model the TB as a poor conductor whose conductivity depends on the relative orientation of the FL and RL magnetization [21]:

$$\sigma_{TB} = \sigma_0 \left(1 + P_{\text{FL}}P_{\text{RL}}\mathbf{m_{RL}} \cdot \mathbf{m_{FL}} \right) \tag{24}$$

$\sigma_0 = (\sigma_{\text{AP}} + \sigma_{\text{P}})/2$ is the average over the conductivities in the parallel and anti-parallel configuration. $\mathbf{m}_{\text{FL/RL}}$ is the FL/RL magnetization. P_{FL} and P_{RL} are Slonczewski polarization parameters related to the TMR through Julliere's formula [22]:

$$\text{TMR} = \frac{R_{\text{AP}} - R_{\text{P}}}{R_{\text{P}}} = \frac{2P_{\text{FL}}P_{\text{RL}}}{1 - P_{\text{FL}}P_{\text{RL}}} \tag{25}$$

R_{AP} and R_P are the resistivities of the anti-parallel and parallel states, respectively.

At the external boundaries not containing an electrode we used the natural assumption of zero flux, i.e. $\mathbf{J_C} \cdot \mathbf{n} = 0, J_S\mathbf{n} = 0$. At boundaries containing an electrode, constant electrical potentials are applied as Dirichlet boundary conditions for the charge current. The spin accumulation gradients normal to the electrodes are assumed to be zero, i.e. $(\nabla \mathbf{S})\mathbf{n} = 0$, resulting in the following Neumann condition for the spin current [23]:

$$J_S\mathbf{n}|_{\text{E}} = -\frac{\mu_B}{e}\beta_\sigma \mathbf{m} \left(\mathbf{J_C} \cdot \mathbf{n} \right) - \theta_{\text{SHA}}\frac{\mu_B}{e}\left(\mathbf{n} \times \mathbf{J_C} \right) \tag{26}$$

The NM contacts are kept long to ensure that the spin accumulation normal to the electrode has sufficiently decayed to zero, sustaining the validity of the no-flux condition.

The tunneling spin current is described by [21,24,25]:

$$J_S\mathbf{n}|_{\text{TB}} = -\frac{\mu_B}{e}\frac{J_C \cdot \mathbf{n}}{1 + P_{\text{RL}}P_{\text{FL}}\mathbf{m_{RL}} \cdot \mathbf{m_{FL}}}$$
$$\times \left[a_{\text{mx}}P_{\text{RL}}\mathbf{m_{RL}} + a_{\text{mx}}P_{\text{FL}}\mathbf{m_{FL}} \right.$$
$$\left. + \frac{1}{2}\left(P_{\text{RL}}P_{\text{RL}}^\eta - P_{\text{FL}}P_{\text{FL}}^\eta \right)\mathbf{m_{RL}} \times \mathbf{m_{FL}} \right] \tag{27}$$

a_{mx} describes the effect of the interface spin-mixing conductance on the transmitted in-plane spin current, and $P_{\text{FL/RL}}^\eta$ is an out-of-plane polarization parameter for the FL/RL.

At NM/FM interfaces we describe the charge and spin currents using magnetoelectronic circuit theory [12,15]:

$$\mathbf{J_C} \cdot \mathbf{n} = \left(G^\uparrow + G^\downarrow \right)\Delta V - \left(G^\uparrow - G^\downarrow \right)\Delta\mathbf{V_S} \cdot \mathbf{m} \tag{28}$$

$$\mathbf{J_S}\mathbf{n} = \frac{\mu_B}{e}\left[2\,\text{Re}\left[G^{\uparrow\downarrow} \right]\mathbf{m} \times (\mathbf{m} \times \Delta\mathbf{V_S}) \right.$$
$$+ 2\,\text{Im}\left[G^{\uparrow\downarrow} \right]\mathbf{m} \times \Delta\mathbf{V_S} - \left(G^\uparrow + G^\downarrow \right)\Delta\mathbf{V_S}$$
$$\left. + \left(G^\uparrow - G^\downarrow \right)\Delta V\mathbf{m} \right] \tag{29}$$

$G^{\uparrow/\downarrow}$ are the interface conductances for the majority/minority spins, while $G^{\uparrow\downarrow}$ is the complex spin-mixing conductance. The interface conductances relate the interface currents to the chemical potential drops across the interface ΔV and $\Delta\mathbf{V_S}$, where the spin chemical potential $\mathbf{V_S} = \frac{e}{\mu_B}\frac{D_e}{\sigma}\mathbf{S}$. The magnetoelectronic circuit theory assumes that the transverse spin current is fully absorbed close to the interface at the FM side [15]; without this assumption (29) needs several modifications in order to get a more general circuit theory. Therefore, we enforce the full absorption of transverse spin currents by keeping λ_ϕ short. At either side of the HM/FM interfaces we include the spin current contribution from the REE which was derived in the previous section:

$$J_S^{\text{R}}\mathbf{n}|_{\text{HM}} = \frac{\mu_B}{e}\sigma_s E_{\text{ip}} \tag{30}$$

$$J_S^{\text{R}}\mathbf{n}|_{\text{FM}} = \frac{\mu_B}{e}\gamma_s^{\text{FM}} E_{\text{ip}} \tag{31}$$

E_{ip} is the magnitude of the in-plane electric field, which we relate to the charge current as follows:

$$E_{\text{ip}} = \frac{\|\mathbf{J_C} - (\mathbf{J_C} \cdot \mathbf{n})\,\mathbf{n}\|}{\sigma} \tag{32}$$

The factor μ_B/e converts the spin current boundary conditions from Section 2 into units of A/s. The terms containing the mixing-conductances should be modified by the interfacial SOC [9,14], however, this modification is considered to be small and to weakly affect the SOTs. It is therefore not treated in this work.

4. Micromagnetic model

We model the magnetization dynamics with the Landau–Lifshitz–Gilbert (LLG) equation for the time evolution of the normalized magnetization $\mathbf{m} = \mathbf{M}/M_S$ [26,27]:

$$\frac{\partial \mathbf{m}}{\partial t} = -\gamma \mu_0 \mathbf{m} \times \mathbf{H_{eff}} + \alpha \mathbf{m} \times \frac{\partial \mathbf{m}}{\partial t} + \frac{1}{M_S} \mathbf{T_S} \tag{33}$$

The first term describes the precession of the magnetization around an effective field $\mathbf{H_{eff}}$, the second term describes the damping of the magnetization towards this field, and the third term describes a spin torque $\mathbf{T_S}$ acting on the magnetization. γ is the gyromagnetic ratio, μ_0 is the vacuum permeability, α is the Gilbert damping constant, and M_S is the saturation magnetization.

By considering the conservation of total spin angular momentum, the spin torque acting on the magnetization obtained from (21) is

$$\mathbf{T_S} = -\frac{D_e}{\lambda_J^2} \mathbf{m} \times \mathbf{S} - \frac{D_e}{\lambda_\phi^2} \mathbf{m} \times (\mathbf{m} \times \mathbf{S}) \tag{34}$$

for a steady state. The spin torques from interfacial SOC are included in the first layer of elements on the FM side of the HM/FM interfaces and are given by:

$$\mathbf{T_S^{int}} = \frac{\mu_B}{e d_h} \gamma_s^{mag} E_{ip} \tag{35}$$

d_h is the thickness of the elements.

We consider the following contributions to the effective field:

$$\mathbf{H_{eff}} = \mathbf{H_{exch}} + \mathbf{H_d} + \mathbf{H_{aniso}} + \mathbf{H_{iDMI}} \tag{36}$$

$\mathbf{H_{exch}}$ is the exchange field, $\mathbf{H_d}$ is the demagnetizing field, $\mathbf{H_{aniso}}$ is the anisotropy field, and $\mathbf{H_{iDMI}}$ is the iDMI field. The exchange field models the exchange interaction between the magnetic moments which favors a parallel orientation and is given by [28]:

$$\mathbf{H_{exch}} = \frac{2A_{ex}}{\mu_0 M_S} \nabla^2 \mathbf{m} \tag{37}$$

A_{ex} is the exchange stiffness coefficient. The demagnetizing field is described by the magnetic potential u through the relation [23]:

$$\mathbf{H_d} = -\nabla u \tag{38}$$

u is obtained by solving the Poisson equation

$$-\nabla^2 u = -M_S \boldsymbol{\nabla} \cdot \mathbf{m} \tag{39}$$

together with the Neumann condition $[(\nabla u) \cdot \mathbf{n}] = -M_S \mathbf{m} \cdot \mathbf{n}$ on the boundaries of the magnetic regions and the constraint of a $\mathcal{O}(1/|\mathbf{r}|)$ decay of u to zero outside the magnetic regions. $[\cdot]$ denotes the discontinuity across the boundary. The Anisotropy field describes the contribution from interface anisotropy and is given by [28]:

$$\mathbf{H_{aniso}} = \frac{2K_{ani}}{\mu_0 M_S} (\mathbf{m} \cdot \mathbf{e_A}) \mathbf{e_A} \tag{40}$$

K_{ani} is the anisotropy coefficient. If $K_{ani} > 0$ then $\mathbf{e_A}$ is the easy-axis, if $K_{ani} < 0$ then $\mathbf{e_A}$ is normal to the easy-plane. The iDMI field models the anti-symmetric exchange interaction in thin FM layers due the strong SOC in adjacent HM layers. It is given by [23,29]:

$$\mathbf{H_{iDMI}} = -\frac{2D_{dmi}}{\mu_0 M_S} (\nabla \times \mathbf{e_D}) \times \mathbf{m} \tag{41}$$

The boundary condition is $(\nabla \mathbf{m})\mathbf{n} = -\frac{D_{dmi}}{2A_{ex}} (\mathbf{e_D} \times \mathbf{n}) \times \mathbf{m}$, where D_{dmi} is the Dzyaloshinskii-Moriya exchange constant and $\mathbf{e_D}$ is the vector orthogonal to the FM layer plane. In contrast to the exchange interaction, the iDMI introduces a favoring of a perpendicular magnetization orientation, which plays an important role for the stabilization of domain walls of the Néel order.

5. Method

We discretize time and compute the partial differential equations (PDEs) using the FEM on a mesh of the problem geometry, with an initial magnetization configuration $\mathbf{m^0}$ at $t = 0$. First, we solve the Laplace equation for the electric potential V and current $\mathbf{J_c}$, the resulting current is then used to solve the continuity equation for the spin accumulation $\mathbf{S}$. From the spin accumulation we obtain the spin torques $\mathbf{T_s}$ entering the LLG. Then, the Possion equation is solved for the magnetic potential, using a hybrid method combining FEM with the boundary element method [30], in order to obtain the demagnetizing field. We solve the LLG for the time derivative of the magnetization $\mathbf{v} = \partial \mathbf{m}/\partial t$ on a sub-mesh containing only the magnetic layers. The time derivative is used to compute the magnetization at the next time iteration $k + 1$.

$$\mathbf{m}^{k+1} = \frac{\mathbf{m}^k + \mathbf{v}^k \delta t}{\|\mathbf{m}^k + \mathbf{v}^k \delta t\|}, \tag{42}$$

δt is the time step. This process then repeats for as many iterations as necessary. For the details of the FEM implementation we refer the reader to [31]. The results were obtained using the open source software ViennaSpinMag [32], extended to include the SHE, REE, and iDMI.

6. Thickness dependence of SOTs

To validate our approach for computing SOTs we compare our results with an analytical derivation which is often employed to model SOTs [12], and the experimental SOT measurements for a Ir/CoFeB bilayer structure reported in [33]. We solve the drift-diffusion equations for the spin accumulation on a mesh of the bilayer structure, with a constant charge current of 5×10^{12} A/m^2 along x and the interface normal along z, and compute the average torque acting on the FM. In order to directly compare our results with the experimental data we convert the computed torques into effective spin torque conductivities, defined as [33]:

$$\begin{aligned} \sigma_{DL}^{eff} &= \frac{2e}{\hbar} \mu_0 M_S t_{FM} \frac{H_{DL}}{E} \\ \sigma_{FL}^{eff} &= \frac{2e}{\hbar} \mu_0 M_S t_{FM} \frac{H_{FL}}{E} \end{aligned} \tag{43}$$

H_{DL} and H_{FL} are the strengths of the effective fields corresponding to the damping-like and field-like torque, respectively. t_{FM} is the thickness of the FM and E is the magnitude of the applied electric field. With the magnetization along $\hat{\mathbf{z}}$, the electric field along $\hat{\mathbf{x}}$, and the HM/FM interface at $z = 0$, we have from (33) that $H_{DL/FL} = \pm T_{DL/FL}/(\gamma \mu_0 M_S)$, where $T_{DL/FL}$ is the torque acting in the damping-like/field-like direction averaged over the FM layer.

Fig. 3 shows the resulting dependence of the spin torque conductivities on the Ir thickness t_{Ir} in a Ir(t_{Ir})/CoFeB(2.3 nm) bilayer structure together with the experimental data and a fit of the analytical expressions. We use the material parameters given in [33] for Ir and the parameters in Table 1 for CoFeB, for the Rashba spin current computation we use the parameters from [12]. We treat θ_{SHA}, Im[$G^{\uparrow\downarrow}$], u_{ex} and u_R as fitting parameters and we obtain a good fit with the experimental data using $\theta_{SHA} = 0.05$, Im[$G^{\uparrow\downarrow}$] $= -0.4 \times 10^{15}$, $u_{ex} = -0.028$ and $u_R = 0.028$. The spin Hall angle of Ir has previously been estimated to be $\theta_{SHA}^{Ir} = 0.02$ [34], however, such measurements also capture several other contributions originating from the interface and defects, which are difficult to separate from the measurement, therefore it is reasonable to assume that the intrinsic spin Hall angle can vary from the measured one.

Panel (a) shows the damping-like spin torque conductivity. The damping-like component increases with the HM thickness until reaching a saturation point which depends on the spin diffusion length. This is a well known result from the literature [9,12]. In this case both
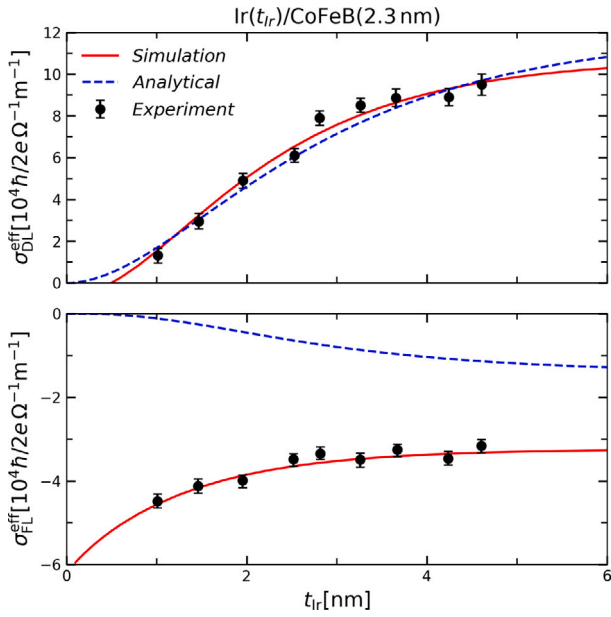
Fig. 3. The dependence of the damping-like (a) and field-like (b) spin torque conductivities on the Ir thickness in a Ir(t_{ir})/CoFeB(2.3 nm) bilayer structure with a current along **x**.

Fig. 4. The angular dependence of the spin torques in a Pt(4.0 nm)/CoFeB(1.2 nm) bilayer structure with a constant charge current density of 5×10^{12} A/m² along x. $m_x = \cos\phi \sin\theta$ and $m_z = \cos\theta$, for the angles $\theta \in [0°, 180°]$ and $\phi \in [0°, 180°]$. The center of each panel corresponds to a magnetization direction along $-y$. The torques are averaged over the volume of the FM layer. Panels (a)–(d), (e)–(h) and (i)–(l), show the SOTs obtained from the SHE, REE and from combining the effects, respectively. The first, second and third column from the left, show the x-, y- and z-component of the SOTs, respectively, while the fourth column shows the magnitude of the torque.

the analytical model and our computations reproduce the experimental data well.

Panel (b) shows the field-like spin torque conductivity. For several HM/FM systems the field-like component has been known to not vanish with decreasing HM thickness [33,35–37], which cannot be explained by only considering the SHE. In this case the simple analytical model fails to reproduce the experimental data as the damping-like component vanishes with decreasing thickness. With the inclusion of the REE in our model we are able to perfectly reproduce this behavior.

7. Magnitude & symmetry of SOTs

We consider a Pt(4 nm)/CoFeB(1.2 nm) bilayer structure with a constant charge current density of 5×10^{12} A/m² along x and the interface normal along z. We express the magnetization in terms of the polar and azimuthal angles θ and ϕ, respectively, yielding the following components $\mathbf{m} = (\cos\phi \sin\theta, \sin\phi \sin\theta, \cos\theta)$. As the bilayer structure we consider is symmetric across the plane spanned by the current and the interface normal vector we compute the torques for $\theta \in [0°, 180°]$ and $\phi \in [0°, 180°]$ to obtain the angular dependence of the SOTs shown in Fig. 4. The material parameters used for Pt and CoFeB are presented in Table 1. The strength of the Rashba SOC is set to $u_R = 0.16$, such that the resulting SOTs are similar in magnitude to the ones obtained from the SHE. The other parameters required for the computation of the REE are again taken from [12]. The computed torques are averaged over the FM and multiplied by a factor of $1/(\gamma M_S)$ in order to obtain the torques in units of T. We consider the case of vanishing REE or SHE, and the combination of both effects. For all cases we observe a vanishing torque, when $m_y = -1$ (center of each panel), which corresponds to the average spin polarization direction. In addition, the x- and z-components change sign when the path of the magnetization passes through $m_y = -1$. This is consistent with the definition of the damping-like and field-like directions the torque can be decomposed into, which describe the damping towards and precession around the spin polarization, respectively. We also observe a 90° rotation of the sign symmetry of the x and z torque components attributed to each effect. From Fig. 3 we know that the damping-like and field-like components dominate for the SHE and REE torques, respectively. This
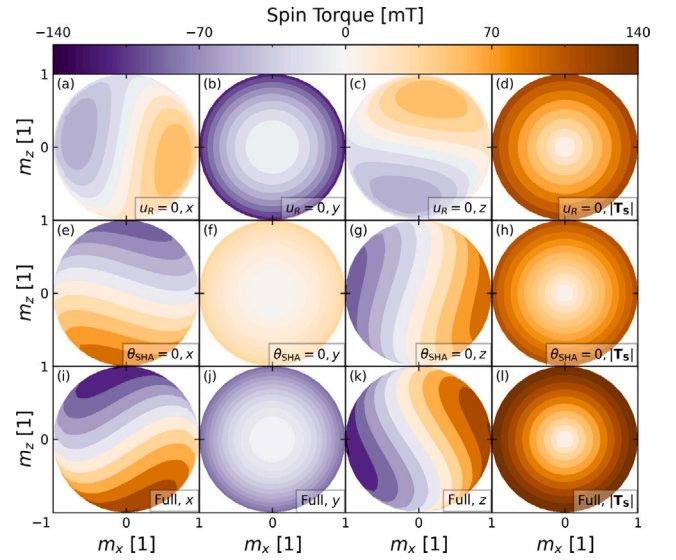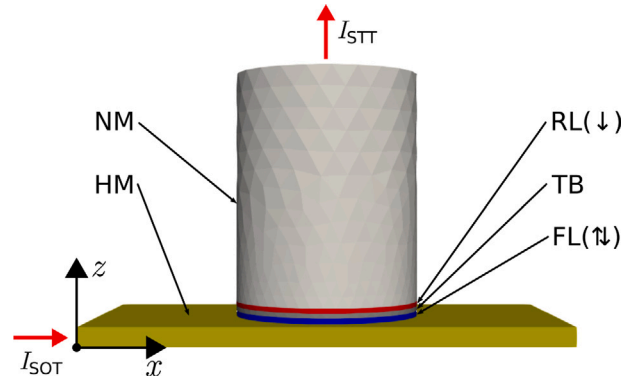
explains the sign symmetry as the two torque directions are orthogonal to each other. When combining both effects, we observe a field-like sign symmetry, as the field-like torque component dominates for our choice of parameters.

8. Modeling hybrid SOT-STT-MRAM

We solve the drift-diffusion equations together with the LLG equation for the time evolution of the FL magnetization on a mesh of a hybrid SOT-STT-MTJ for 1 ns using a time step of 10^{-4} ns, the mesh is depicted in Fig. 5. The mesh contains a perpendicular MTJ, with a top contact placed on a HM SOT track. The RL magnetization is fixed along $-z$. The initial FL magnetization is in an anti-parallel alignment, i.e. along z. A voltage of 0.15 V and 2.0 V is applied at the SOT (lower left) and STT (top) contact, respectively, while the lower right contact is kept grounded. The SOT voltage is applied for the first 0.4 ns. The material parameters used are presented in Table 1, which correspond to Pt, MgO, and CoFeB for the HM, TB, and FM layers, respectively. A
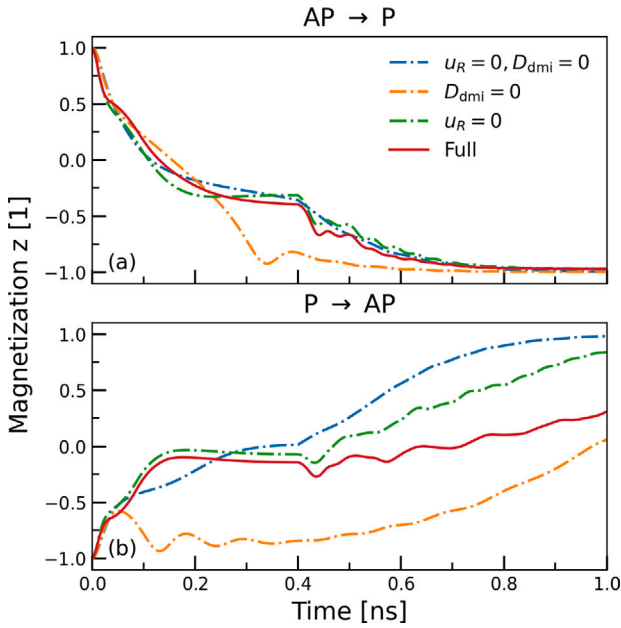

Fig. 5. A mesh of an out-of-plane SOT-MTJ stack Pt(4.0 nm)/CoFeB(1.2 nm)/MgO(1.0 nm)/CoFeB(1.0 nm). The HM layer has a surface area of 100×50 nm², while the MTJ has a diameter of 20 nm.

Fig. 6. The average z-component of the normalized magnetization $\mathbf{m}$ as a function of time computed on the mesh depicted in Fig. 5. The upper and lower panels show APP and PAP switching, respectively.

Fig. 7. Evolution of the z-component of the FL magnetization during the APP switching process.

strong Rashba SOC ($u_R = 0.16$) is used in order to magnify its influence on the switching.

Fig. 6 shows the evolution of the z-component of the FL magnetization averaged over the FL during APP and PAP switching. We also consider the cases of vanishing interfacial Rashba SOC and iDMI, to better understand the role of these effects during the reversal of the FL magnetization. The magnetization dynamics are similar in all the considered scenarios, except for the case of vanishing iDMI and strong Rashba SOC. During the first 0.4 ns the magnetization is quickly brought in-plane by the SOTs, followed by the slower completion of the switching with the STTs after the SOT current has been turned off. The inclusion of REE contributes to bringing the magnetization in-plane during the SOT phase for APP switching, as the total torque is stronger. Furthermore, in the case of vanishing iDMI, the Rashba torque switches the FL completely in the SOT-phase. However, for the PAP switching, the Rashba torque works against the switching and for vanishing iDMI the magnetization is not brought in-plane in the SOT-phase. After the SOT pulse, the contribution from the REE effect vanishes as there are no longer in-plane currents along the HM/FM interface. The inclusion of the iDMI shows a large impact on the switching process, as it introduces a favoring of a canted magnetization configuration. This assists the magnetization in reaching the in-plane state, overcoming the strong Rashba torques in PAP switching. However, it also makes reaching a parallel (anti-parallel) final configuration more difficult, as the iDMI works against the switching after the in-plane configuration has been reached.

Fig. 7 shows several time snapshots of the FL magnetization during APP switching. During the SOT phase a domain wall is nucleated at the top ($y = 40$ nm) side of the FL, which propagates towards the center, bringing the average magnetization in-plane. This agrees well with the observations reported in [38]. During the STT phase the domain wall begins to precess around the edge of the FL while shrinking, until the whole FL magnetization has switched. Without the inclusion of the iDMI, no domain walls are observed, and instead a homogeneous magnetization reversal occurs across the whole FL.

9. Modeling of SOT-MRAM with built-in in-plane field

We solve the system of equations on the mesh depicted in Fig. 8 for 1 ns using a time step of $h = 10^{-4}$ ns. The additional FM underneath the
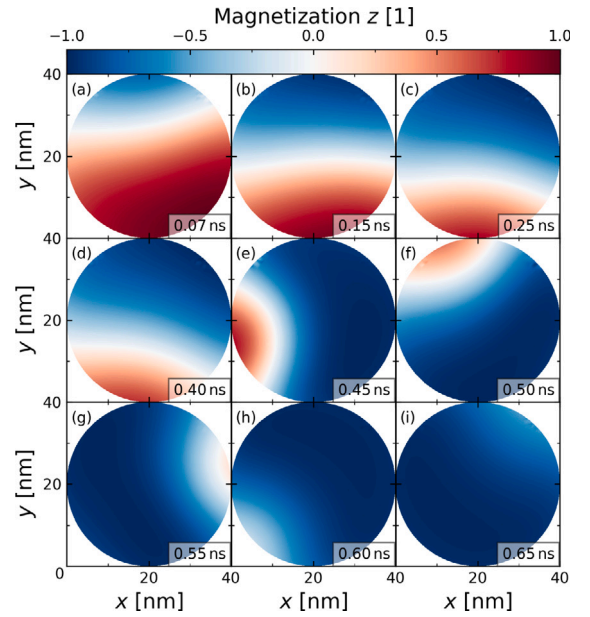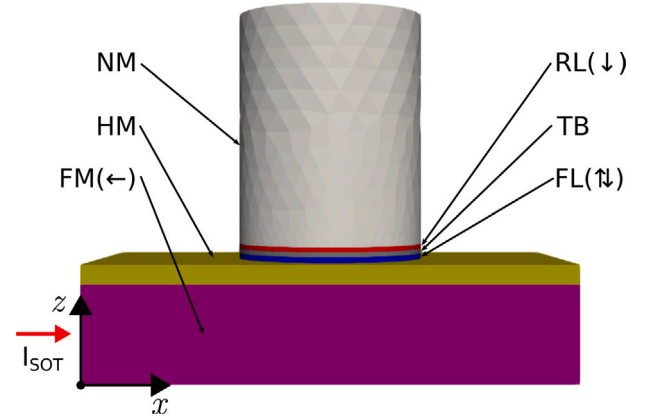

Fig. 8. A mesh of an out-of-plane SOT-MTJ stack Pt(4.0 nm)/CoFeB(1.2 nm)/MgO (1.0 nm)/CoFeB(1.0 nm), with an additional FM(20.0 nm) layer underneath the HM with a fixed magnetization along $-x$. The HM layer has a surface area of 100×50 nm^2, while the MTJ has a diameter of 20 nm.

HM has a fixed in-plane magnetization along $-x$ and generates a stray field along x in the FL which breaks the symmetry of the SOTs, similarly to an external field. In this case no voltage is applied at the top contact, while a 0.15 V bias is applied across the HM/IP-FM bilayer structure. The material parameters are the same as in the previous section, except for a $\times 1.5$ higher M_S in the additional in-plane FM layer to generate a strong enough stray field to complete the switching.

The z-component of the FL magnetization averaged over the FL is shown in Fig. 9 during APP and PAP switching.

We observe that in all cases the magnetization is reversed. However, with the inclusion of iDMI and vanishing Rashba SOC, the switching does not fully complete, and stabilizes at $m_z \approx \pm 0.5$, as the in-plane favoring is strong enough to prevent full switching from being achieved. As the spin torque also favors the in-plane configuration, turning off the current should help the magnetization relax to a fully switched orientation, otherwise, a stronger stray field might be required to fully complete the switching.

With the inclusion of the REE the switching is improved, and the stable intermediate state introduced by the iDMI is overcome and
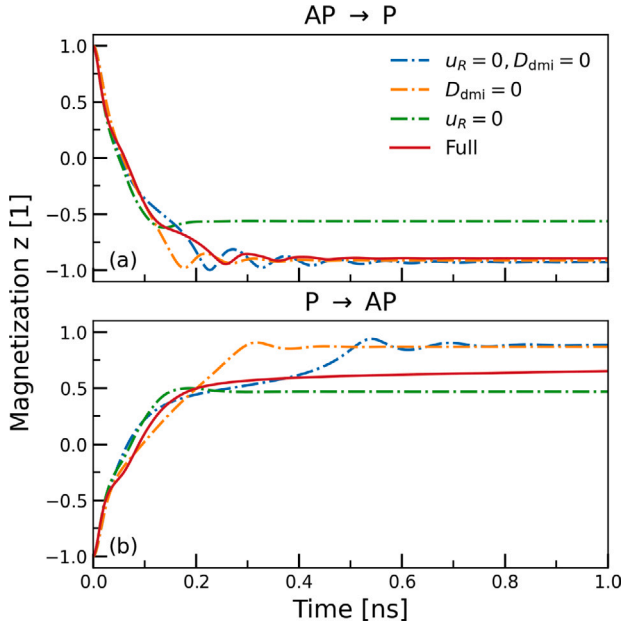
Fig. 9. The average z-component of the normalized magnetization **m** as a function of time computed on the mesh depicted in Fig. 8. The upper and lower panels show APP and PAP switching, respectively.

Table 1
Material parameters.

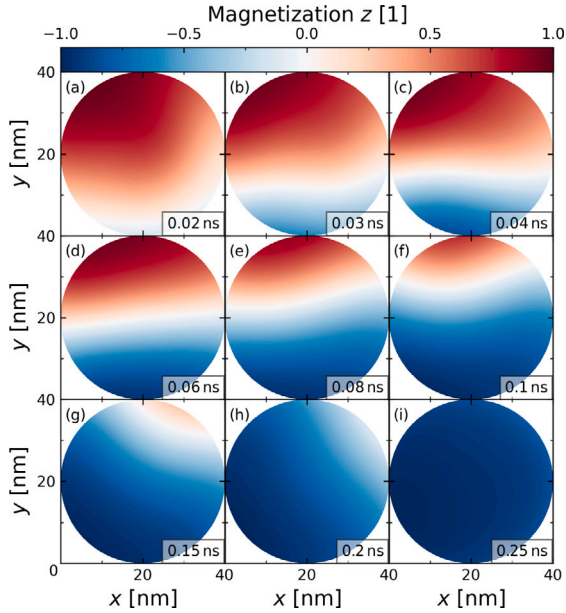| Parameter	Value
LLG (CoFeB)	
Gilbert damping, α	0.02
Saturation magnetization, M_S	0.81×10^6 A m^{-1}
Exchange stiffness, A_{exch}	2×10^{-11} J m^{-1}
Anisotropy energy density, K_{ani}	0.545×10^6 J m^{-3}
DMI energy, D_{dmi}	-1.75×10^{-3} J m^{-2}
Drift-Diffusion (CoFeB & Pt & MgO)	
Conductivity FM, σ^{FM}	4×10^6 Sm^{-1}
Conductivity NM, σ^{NM}	7×10^6 Sm^{-1}
Diffusion Coefficient FM, D_e^{FM}	10^{-2} m^{2}s^{-1}
Diffusion Coefficient NM, D_e^{NM}	1.1×10^{-3} m^2 s^{-1}
Spin-flip length FM, λ_{sf}^{FM}	10 nm
Spin-flip length NM, λ_{sf}^{NM}	1.4 nm
Spin exchange length, λ_J	0.8 nm
Spin dephasing length, λ_ϕ	0.4 nm
Conductivity polarization, β_σ	0.52
Diffusion polarization, β_D	0.7
Spin Hall angle, θ_{SHA}	0.19
Tunnel magnetoresistance ratio	200%
Resistance parallel, R_P	1.4×10^4 Ω
Resistance anti-parallel, R_{AP}	4.2×10^4 Ω
Majority spin conductance, $G^\uparrow$	1.0×10^{15} Sm^{-2}
Minority spin conductance, $G^\downarrow$	0.1×10^{15} Sm^{-2}
Spin-mixing conductance, Re$\{G^{\uparrow\downarrow}\}$	2.0×10^{15} Sm^{-2}
Spin-mixing conductance, Im$\{G^{\uparrow\downarrow}\}$	0.7×10^{15} Sm^{-2}

Fig. 10. Evolution of the z-component of the FL magnetization during the APP switching process.

full switching is achieved. As the symmetry of the REE torques in a bilayer structure should also favor the in-plane configuration, this suggest that the REE spin currents generated at the HM/IP-FM interface exert a torque on the FL magnetization which has an unconventional symmetry.

Fig. 10 shows snapshots of the FL magnetization during APP switching.

We observe a domain wall nucleating from the side of the FL at a $-45°$ angle with the current direction, which propagates across the FL. As the stray field breaks the symmetry of the SOTs, the domain wall

continues to propagate and vanishes in the lower right corner at a 45° angle from the center, completing the switching. Similar domain wall propagations were also reported in [38], with the exception that the domain walls were shown to propagate along a straight line. However, a different structure was used, and an external field along the current direction was used instead of a built-in one.

10. Conclusion

We have presented a new approach for modeling of the magnetization dynamics in SOT-MRAM cells. We have generalized the expressions from [10] for an arbitrary magnetization direction and derived analytical expression for the scattering matrices, resulting in boundary condition that can capture the complex REE effect at HM/FM interfaces. Through the inclusion of spin–orbital effects into the coupled charge and spin drift-diffusion equations, we can compute the spin torques originating from the SHE and REE acting on the magnetic layers of multi-layer structures. We show that in HM/FM bilayer structures we can reproduce experimental results for the SOTs. We have shown that including the torques in the LLG equation, together with important effective field contributions such as the demagnetizing and iDMI field, enables the modeling of the complex magnetization reversal of the FL. We have demonstrated the flexibility of our approach by simulating two different approaches for field-free SOT-pMTJs. Using relevant material parameters we are able to reproduce the general behavior of these devices.

CRediT authorship contribution statement

Nils Petter Jørstad: Conceptualization, Data curation, Formal analysis, Investigation, Methodology, Software, Visualization, Writing – original draft, Writing – review & editing. **Simone Fiorentini:** Software, Writing – review & editing. **Johannes Ender:** Software, Writing – review & editing. **Wolfgang Goes:** Software, Writing – review & editing. **Siegfried Selberherr:** Supervision, Writing – review & editing. **Viktor Sverdlov:** Conceptualization, Supervision, Project administration, Funding acquisition, Writing – review & editing.

Declaration of competing interest

The authors declare that they have no known competing financial interests or personal relationships that could have appeared to influence the work reported in this paper.

Data availability

Data will be made available on request.

Appendix A. Scattering matrices

We compute the traces in Eqs. (7) and (8) using the scattering amplitudes for the spin-dependent interface potential in Eqs. (5) and (6), respectively. The resulting Boltzmann scattering matrices have the following block-diagonal form:

$$\overline{S} = \begin{pmatrix} a_v & b_v & 0 & 0 \\ -b_v & a_v & 0 & 0 \\ 0 & 0 & c & d \\ 0 & 0 & d & c \end{pmatrix}, \tag{A.1}$$

$v \in \{r, t\}$ denotes the matrix element for reflection (r) or transmission (t). The elements in the lower right block are the same for both matrices. The resulting matrix elements can be written as follows:

$$a_r = \cos(\chi_\uparrow - \chi_\downarrow)\cos(\chi_\uparrow)\cos(\chi_\downarrow) \tag{A.2a}$$

$$b_r = \sin(\chi_\uparrow - \chi_\downarrow)\cos(\chi_\uparrow)\cos(\chi_\downarrow) \tag{A.2b}$$

$$a_t = \cos(\chi_\uparrow - \chi_\downarrow)\sin(\chi_\uparrow)\sin(\chi_\downarrow) \tag{A.2c}$$

$$b_t = \sin(\chi_\uparrow - \chi_\downarrow)\sin(\chi_\uparrow)\sin(\chi_\downarrow) \tag{A.2d}$$

$$c = \frac{\sin(\chi_\uparrow)\sin(\chi_\uparrow) + \sin(\chi_\downarrow)\sin(\chi_\downarrow)}{2} \tag{A.2e}$$

$$d = \frac{\sin(\chi_\uparrow)\sin(\chi_\uparrow) - \sin(\chi_\downarrow)\sin(\chi_\downarrow)}{2} \tag{A.2f}$$

The angle $\chi^{\uparrow/\downarrow}$ is defined as:

$$\chi^{\uparrow/\downarrow} = \tan^{-1}\left(\frac{k_z/k_F}{u^{\uparrow/\downarrow}}\right) \tag{A.3}$$

Appendix B. Orthogonal transformation for the spin basis

With the interface normal along $\hat{z}$ and the electric field along $\hat{x}$, we define the spin basis with the following set of orthogonal vectors:

$$\hat{x}'(\mathbf{k}) = \hat{u}_{\text{Eff}}(\mathbf{k}) \times (\hat{z} \times \hat{x}) \tag{B.1a}$$

$$\hat{y}'(\mathbf{k}) = \hat{u}_{\text{Eff}}(\mathbf{k}) \times \left(\hat{u}_{\text{Eff}}(\mathbf{k}) \times (\hat{z} \times \hat{x})\right) \tag{B.1b}$$

$$\hat{z}'(\mathbf{k}) = \hat{u}_{\text{Eff}}(\mathbf{k}) \tag{B.1c}$$

The orthogonal transformation matrix from the spin basis to the frame aligned with the interface and current is then given by:

$$O_{\mathbf{s}}(\mathbf{k}) = \begin{bmatrix} \hat{x}'(\mathbf{k}) & \hat{y}'(\mathbf{k}) & \hat{z}'(\mathbf{k}) \end{bmatrix} \tag{B.2}$$

The 4×4 transformation matrix is then given by:

$$O(\mathbf{k}) = \begin{pmatrix} O_{\mathbf{s}}(\mathbf{k}) & 0 \\ 0 & 1 \end{pmatrix} \tag{B.3}$$

In the limit of no SOC ($u_R \to 0$), $\hat{x}'$ and $\hat{y}'$ reduce to the damping-like and field-like directions, respectively, while $\hat{z}'$ becomes aligned with $\mathbf{m}$.

Appendix C. Orthogonal transformation for generalized spin transport

In order to generalize the REE spin current and torque contribution calculations in Section 2 to any direction of the interface normal $\mathbf{n}$ and in-plane electric field $\hat{E}_{\text{ip}}$, additional coordinate transformations are required between the laboratory frame and the interface calculation frame where $\mathbf{n} = \hat{z}$ and $\hat{E}_{\text{ip}} = \hat{x}$. We define the interface calculation basis with the following set of orthogonal vectors:

$$\hat{x}_{\text{int}} = \hat{E} - (\hat{E} \cdot \mathbf{n})\mathbf{n} = \hat{E}_{\text{ip}} \tag{C.1a}$$

$$\hat{y}_{\text{int}} = \mathbf{n} \times \hat{E} \tag{C.1b}$$

$$\hat{z}_{\text{int}} = \mathbf{n} \tag{C.1c}$$

The orthogonal transformation from the laboratory frame to the interface calculation frame is then given by:

$$O_{\text{int}} = \begin{bmatrix} \hat{x_{\text{int}}} & \hat{y_{\text{int}}} & \hat{z_{\text{int}}} \end{bmatrix} \tag{C.2}$$

The magnetization used in the interface calculations m_{int} is then obtained with

$$m^{\text{int}} = O_{\text{int}}\mathbf{m} \tag{C.3}$$

and the conductivity and torkivity tensors used in the drift-diffusion equations are given by

$$\sigma_s = O_{\text{int}}^T \sigma_s^{\text{int}} \tag{C.4}$$

and

$$\gamma_s = O_{\text{int}}^T \gamma_s^{\text{int}}, \tag{C.5}$$

respectively.

References

[1] F. Oboril, R. Bishnoi, M. Ebrahimi, M.B. Tahoori, Evaluation of hybrid memory technologies using SOT-MRAM for on-chip cache hierarchy, IEEE Trans. Comput.-Aided Des. Integr. Circuits Syst. 34 (3) (2015) 367–380, http://dx.doi.org/10.1109/TCAD.2015.2391254.

[2] Q. Shao, P. Li, L. Liu, H. Yang, S. Fukami, A. Razavi, H. Wu, K. Wang, F. Freimuth, Y. Mokrousov, M.D. Stiles, S. Emori, A. Hoffmann, J. Åkerman, K. Roy, J.-P. Wang, S.-H. Yang, K. Garello, W. Zhang, Roadmap of spin–orbit torques, IEEE Trans. Magn. 57 (7) (2021) 1–39, http://dx.doi.org/10.1109/TMAG.2021.3078583.

[3] R. Saha, Y.P. Pundir, P. Kumar Pal, Comparative analysis of STT and SOT based MRAMs for last level caches, J. Magn. Magn. Mater. 551 (2022) 169161, http://dx.doi.org/10.1016/j.jmmm.2022.169161.

[4] J. Sinova, S.O. Valenzuela, J. Wunderlich, C.H. Back, T. Jungwirth, Spin Hall effects, Rev. Modern Phys. 87 (2015) 1213–1260, http://dx.doi.org/10.1103/RevModPhys.87.1213.

[5] V. Edelstein, Spin polarization of conduction electrons induced by electric current in two-dimensional asymmetric electron systems, Solid State Commun. 73 (3) (1990) 233–235, http://dx.doi.org/10.1016/0038-1098(90)90963-C.

[6] K. Garello, F. Yasin, H. Hody, S. Couet, L. Souriau, S.H. Sharifi, J. Swerts, R. Carpenter, S. Rao, W. Kim, J. Wu, K.K.V. Sethu, M. Pak, N. Jossart, D. Crotti, A. Furnémont, G.S. Kar, Manufacturable 300 mm platform solution for field-free switching SOT-MRAM, in: Symposium on VLSI Circuits, 2019, pp. T194–T195, http://dx.doi.org/10.23919/VLSIC.2019.8778100.

[7] A. Razavi, H. Wu, Q. Shao, C. Fang, B. Sai, K. Wong, X. Han, G. Yu, K.L. Wang, Deterministic spin–orbit torque switching by a light-metal insertion, Nano Lett. 20 (2020) 3703–3709, http://dx.doi.org/10.1021/acs.nanolett.0c00647.

[8] M. Wang, W. Cai, D. Zhu, Z. Wang, J. Kan, Z. Zhao, K. Cao, Z. Wang, Y. Zhang, T. Zhang, C. Park, J.-P. Wang, A. Fert, W. Zhao, Field-free switching of a perpendicular magnetic tunnel junction through the interplay of spin–orbit and spin-transfer torques, Nat. Electron. 1 (2018) 582–588, http://dx.doi.org/10.1038/s41928-018-0160-7.

[9] V.P. Amin, M.D. Stiles, Spin transport at interfaces with spin-orbit coupling: Phenomenology, Phys. Rev. B 94 (2016) 104420, http://dx.doi.org/10.1103/PhysRevB.94.104420.

[10] V.P. Amin, P.M. Haney, M.D. Stiles, Interfacial spin–orbit torques, J. Appl. Phys. 128 (15) (2020) 151101, http://dx.doi.org/10.1063/5.0024019.

[11] H. Kurebayashi, J. Sinova, D. Fang, A.C. Irvine, T.D. Skinner, J. Wunderlich, V. Novák, R.P. Campion, B.L. Gallagher, E.K. Vehstedt, L.P. Zârbo, K. Výborný, A.J. Ferguson, T. Jungwirth, An antidamping spin–orbit torque originating from the Berry curvature, Nature Nanotechnol. 9 (2014) 211–217, http://dx.doi.org/10.1038/nnano.2014.15.

[12] P.M. Haney, H.-W. Lee, K.-J. Lee, A. Manchon, M.D. Stiles, Current induced torques and interfacial spin-orbit coupling: Semiclassical modeling, Phys. Rev. B 87 (2013) 174411, http://dx.doi.org/10.1103/PhysRevB.87.174411.

[13] K.-W. Kim, K.-J. Lee, J. Sinova, H.-W. Lee, M.D. Stiles, Spin-orbit torques from interfacial spin-orbit coupling for various interfaces, Phys. Rev. B 96 (10) (2017) http://dx.doi.org/10.1103/physrevb.96.104438.

[14] V.P. Amin, M.D. Stiles, Spin transport at interfaces with spin-orbit coupling: Formalism, Phys. Rev. B 94 (2016) 104419, http://dx.doi.org/10.1103/PhysRevB.94.104419.

[15] A. Brataas, G.E. Bauer, P.J. Kelly, Non-collinear magnetoelectronics, Phys. Rep. 427 (4) (2006) 157–255, http://dx.doi.org/10.1016/j.physrep.2006.01.001.

[16] S. Lepadatu, Unified treatment of spin torques using a coupled magnetisation dynamics and three-dimensional spin current solver, Sci. Rep. 7 (1) (2017) 12937, http://dx.doi.org/10.1038/s41598-017-13181-x.

[17] C. Abert, M. Ruggeri, F. Bruckner, C. Vogler, G. Hrkac, D. Praetorius, D. Suess, A three-dimensional spin-diffusion model for micromagnetics, Sci. Rep. 5 (1) (2015) 14855, http://dx.doi.org/10.1038/srep14855.

[18] C. Petitjean, D. Luc, X. Waintal, Unified drift-diffusion theory for transverse spin currents in spin valves, domain walls, and other textured magnets, Phys. Rev. Lett. 109 (2012) 117204, http://dx.doi.org/10.1103/PhysRevLett.109.117204.

[19] S. Zhang, P.M. Levy, A. Fert, Mechanisms of spin-polarized current-driven magnetization switching, Phys. Rev. Lett. 88 (2002) http://dx.doi.org/10.1103/PhysRevLett.88.236601.

[20] M. Ruggeri, C. Abert, G. Hrkac, D. Suess, D. Praetorius, Coupling of dynamical micromagnetism and a stationary spin drift-diffusion equation: A step towards a fully self-consistent spintronics framework, Physica B 486 (2016) 88–91, http://dx.doi.org/10.1016/j.physb.2015.09.003.

[21] S. Fiorentini, M. Bendra, J. Ender, R. L. de Orio, W. Goes, S. Selberherr, V. Sverdlov, Spin and charge drift-diffusion in ultra-scaled MRAM cells, Sci. Rep. 12 (2022) http://dx.doi.org/10.1038/s41598-022-25586-4.

[22] M. Julliere, Tunneling between ferromagnetic films, Phys. Lett. A 54 (3) (1975) 225–226, http://dx.doi.org/10.1016/0375-9601(75)90174-7.

[23] C. Abert, Micromagnetics and spintronics: models and numerical methods, Eur. Phys. J. B 92 (6) (2019) http://dx.doi.org/10.1140/epjb/e2019-90599-6.

[24] K.Y. Camsari, S. Ganguly, D. Datta, S. Datta, Physics-based factorization of Magnetic Tunnel Junctions for modeling and circuit simulation, in: IEEE International Electron Devices Meeting, 2014, pp. 35.6.1–35.6.4, http://dx.doi.org/10.1109/IEDM.2014.7047177.

[25] M. Chshiev, A. Manchon, A. Kalitsov, N. Ryzhanova, A. Vedyayev, N. Strelkov, W. Butler, B. Dieny, Analytical description of ballistic spin currents and torques in magnetic tunnel junctions, Phys. Rev. B 92 (2015) 104422, http://dx.doi.org/10.1103/PhysRevB.92.104422.

[26] T. Gilbert, A phenomenological theory of damping in ferromagnetic materials, IEEE Trans. Magn. 40 (6) (2004) 3443–3449, http://dx.doi.org/10.1109/TMAG.2004.836740.

[27] J. Xiao, A. Zangwill, M.D. Stiles, Macrospin models of spin transfer dynamics, Phys. Rev. B 72 (1) (2005) http://dx.doi.org/10.1103/physrevb.72.014446.

[28] J.E. Miltat, M.J. Donahue, Handbook of Magnetism and Advanced Magnetic Materials, John Wiley & Sons, Ltd, 2007, pp. 1–22, http://dx.doi.org/10.1002/9780470022184.hmm202, Ch. Numerical Micromagnetics: Finite Difference Methods.

[29] G. Hrkac, C.-M. Pfeiler, D. Praetorius, M. Ruggeri, A. Segatti, B. Stiftner, Convergent tangent plane integrators for the simulation of chiral magnetic skyrmion dynamics, Adv. Comput. Math. 45 (3) (2019) 1329–1368, http://dx.doi.org/10.1007/s10444-019-09667-z.

[30] J. Ender, M. Mohamedou, S. Fiorentini, R. Orio, S. Selberherr, W. Goes, V. Sverdlov, Efficient demagnetizing field calculation for disconnected complex geometries in STT-MRAM cells, in: 2020 International Conference on Simulation of Semiconductor Processes and Devices, SISPAD, 2020, pp. 213–216, http://dx.doi.org/10.23919/SISPAD49475.2020.9241662.

[31] S. Fiorentini, N.P. Jørstad, J. Ender, R.L. de Orio, S. Selberherr, M. Bendra, W. Goes, V. Sverdlov, Finite element approach for the simulation of modern MRAM devices, Micromachines 14 (5) (2023) http://dx.doi.org/10.3390/mi14050898.

[32] CDL NovoMemLog, ViennaSpinMag, 2022, URL https://www.iue.tuwien.ac.at/viennaspinmag/.

[33] S. Dutta, A. Bose, A.A. Tulapurkar, R.A. Buhrman, D.C. Ralph, Interfacial and bulk spin Hall contributions to fieldlike spin-orbit torque generated by iridium, Phys. Rev. B 103 (2021) 184416, http://dx.doi.org/10.1103/PhysRevB.103.184416.

[34] T. Fache, J.C. Rojas-Sanchez, L. Badie, S. Mangin, S. Petit-Watelot, Determination of spin Hall angle, spin mixing conductance, and spin diffusion length in CoFeB/Ir for spin-orbitronic devices, Phys. Rev. B 102 (2020) 064425, http://dx.doi.org/10.1103/PhysRevB.102.064425.

[35] A. Ghosh, K. Garello, C.O. Avci, M. Gabureac, P. Gambardella, Interface-enhanced spin-orbit torques and current-induced magnetization switching of Pd/Co/AlO$_x$ layers, Phys. Rev. A 7 (2017) 014004, http://dx.doi.org/10.1103/PhysRevApplied.7.014004.

[36] A.J. Berger, E.R.J. Edwards, H.T. Nembach, O. Karis, M. Weiler, T.J. Silva, Determination of the spin Hall effect and the spin diffusion length of Pt from self-consistent fitting of damping enhancement and inverse spin-orbit torque measurements, Phys. Rev. B 98 (2018) 024402, http://dx.doi.org/10.1103/PhysRevB.98.024402.

[37] L. Zhu, D.C. Ralph, R.A. Buhrman, Maximizing spin-orbit torque generated by the spin Hall effect of Pt, Appl. Phys. Rev. 8 (3) (2021) http://dx.doi.org/10.1063/5.0059171.

[38] M. Baumgartner, K. Garello, J. Mendil, C.O. Avci, E. Grimaldi, C. Murer, J. Feng, M. Gabureac, C. Stamm, Y. Acremann, S. Finizio, S. Wintz, J. Raabe, P. Gambardella, Spatially and time-resolved magnetization dynamics driven by spin–orbit torques, Nature Nanotechnol. 12 (10) (2017) 980–986, http://dx.doi.org/10.1038/nnano.2017.151.